Image-Based Computational Fluid Dynamics in Blood Vessel Models: Toward Developing a Prognostic Tool to Assess Cardiovascular Function Changes in Prolonged Space Flights

George P. Chatzimavroudis[*a,b], Thomas A. Spirka[a], Randolph M. Setser[b], Jerry G. Myers[c]

[a]Department of Chemical and Biomedical Engineering, Cleveland State University, Cleveland, OH;
[b]Division of Radiology, The Cleveland Clinic Foundation, Cleveland, OH
[c]Human Health and Performance Office, NASA Glenn Research Center, Cleveland, OH;

ABSTRACT

One of NASA's objectives is to be able to perform a complete, pre-flight evaluation of possible cardiovascular changes in astronauts scheduled for prolonged space missions. Blood flow is an important component of cardiovascular function. Computational fluid dynamics (CFD) has shown promise as a flow analysis method. Lately, attention has focused on reconstructing realistic vessel geometries. MRI can provide detailed geometrical information and is the only clinical technique to measure all three spatial velocity components. The objective of this study was to investigate the reliability of MRI-based model reconstruction for CFD simulations. An aortic arch model and a carotid bifurcation model were scanned in a 1.5T Siemens MRI scanner. Axial MRI acquisitions provided images for geometry reconstruction; using different resolution settings (slice thickness 3 and 5 mm; pixel size 1x1 and 0.5x0.5 mm^2). The vessel walls were specified using ImageJ and the geometry was reconstructed using Rhinoceros. The geometry was then imported into CFD-GEOM for meshing, before executing the simulation with CFD-ACE. MRI velocity acquisitions provided true inlet boundary conditions for steady flowrates between 0.7 and 3.0 L/min, as well as three-directional velocity data at several vessel locations. In addition, an idealized version of each geometry was created from the model drawings. Contour and vector plots of the velocity showed identical features between the MRI velocity data, the MRI-based CFD data, and the idealized-geometry CFD data, with <10% differences in the local velocity values. CFD results on reconstructed models from different MRI resolution settings did not show significant differences (<5%). This study showed quantitatively that reliable CFD simulations can be performed in models reconstructed from MRI acquisitions and gives evidence that a future, subject-specific, computational evaluation of the cardiovascular system is possible.

1. INTRODUCTION

In February of 2004 the National Aeronautics and Space Administration (NASA) released a report entitled The Vision for Space Exploration that sets the year 2015 as a target date for conducting an extended human expedition to the moon. This moon mission and other subsequent missions will serve as a test platform to develop the technology to eventually conduct human expeditions to Mars and beyond.[1] One of the major challenges that must be overcome prior to this date and a priority of NASA is to identify and study possible risks to astronauts' health that will be encountered during prolonged space missions.[2] One of NASA's aims is to develop a procedure that would allow for the pre-flight evaluation of potential astronauts' cardiovascular systems, in order to determine how each individual's cardiovascular system will be affected by the stresses encountered during a prolonged space mission. In order to be able to make this predication, a computational model must be constructed based on each individual's specific anatomy and physiology in order to subject the model to the stresses that an astronaut would face with out endangering the health of the astronaut. Currently a method for building such a model of a patient specific cardiovascular system does not exist. However, several recent studies investigating the role of blood flow in the development and progression of the disease atherosclerosis have published various methods in which medical images are used to construct computational models of either in vitro flow phantoms or in vivo blood vessels. The flow patterns and various other aspects of the flow fields are then predicted through the use of a commercial computational fluid dynamics software package. In line with these studies investigating the role of blood flow in atherosclerosis a large number of these studies including studies by Steinman et al[3, 4], Long et al[5], Botnar et al[6], Zhao et al[7], and Marshall et al[8] have focused almost exclusively on the carotid artery specifically the area where the common carotid artery bifurcates into the internal and external carotid arteries. Only a very small number of studies have focused on the other major vessels of the cardiovascular system. Leuprecht et al focused on the ascending aorta[9]. Wood et al focused on the descending aorta[10]. Glor et al focused on a

planar U-bend phantom that simulated flow in the aorta[11]. Long et al[12] and Moore et al[13] focused on the region where the abdominal aorta bifurcates into the iliac arteries (Should include The relationship between wall shear stress distributions and intimal thickening in the human abdominal aorta Michael Bonert1,2, Richard L Leask1,2,3, Jagdish Butany4, C Ross Ethier1,2, Jerry G Myers1,2, K Wayne Johnston2,5 and Matadial Ojha*1,2 BioMedical Engineering OnLine 2003, 2:18). All of the above mentioned studies use a common general method in that the artery or phantom of interest is imaged typically using Magnetic Resonance Imaging (MRI) or computer Tomography (CT). The resulting images are segmented in some way to yield the geometric data for the vessel of interest. The geometric data obtained is then used to construct a computational model which is then meshed and solved using a computational fluid dynamics program.   MRI has become the imaging modality of choice as only this modality can be used to obtain both the geometric information required to construct the computational models as well as the three dimensional velocity data required to provide accurate boundary conditions and to validate the CFD predictions.   Studies using medical image based CFD have focused primarily on achieving qualitative agreement between CFD predictions and MRI measurements. Only a small number of recent studies including studies by Steinman et al[4] and Zhao et al[14] have been published recently in which quantitative comparisons have been made between MRI measurements and CFD Predictions with regard to flow in a carotid bifurcation geometry.

The main goal of the present work is to investigate the reliability of CFD predictions for models constructed from MRI images. An aortic arch and planar carotid flow phantom were imaged under steady flow conditions. Computational models were then reconstructed from the images and solved using a commercial computational fluid dynamics package. The results were then compared to MRI velocity measurements both qualitatively and quantitatively in order to determine the accuracy of the computational models. In addition idealized computational models were constructed for both phantoms using only the dimensions supplied to the manufacturer of the flow phantoms in order to determine if the MRI generated models would be more accurate in predicting flow patterns and localized velocities.

2.   METHODOLOGY

2.1 Flow Phantoms

Two flow phantoms (Technical Glass Products Inc, Painseville, OH) were used in the current study the first shown in Figure 1 was designed based on the dimensions of a simplified aortic arch. A constant inner diameter of one inch was specified for the entire phantom. (The actual I.D. for the manufactured phantom was approximately three one hundredths of an inch (the units here are inconsistent with the units used throughout the rest of the paper, these should be converted to SI) undersized from the specified diameter.) A non-planar (20-degree out of plane) arch having a three quarter inch radius of curvature connected the ascending and descending portions of the aortic phantom.
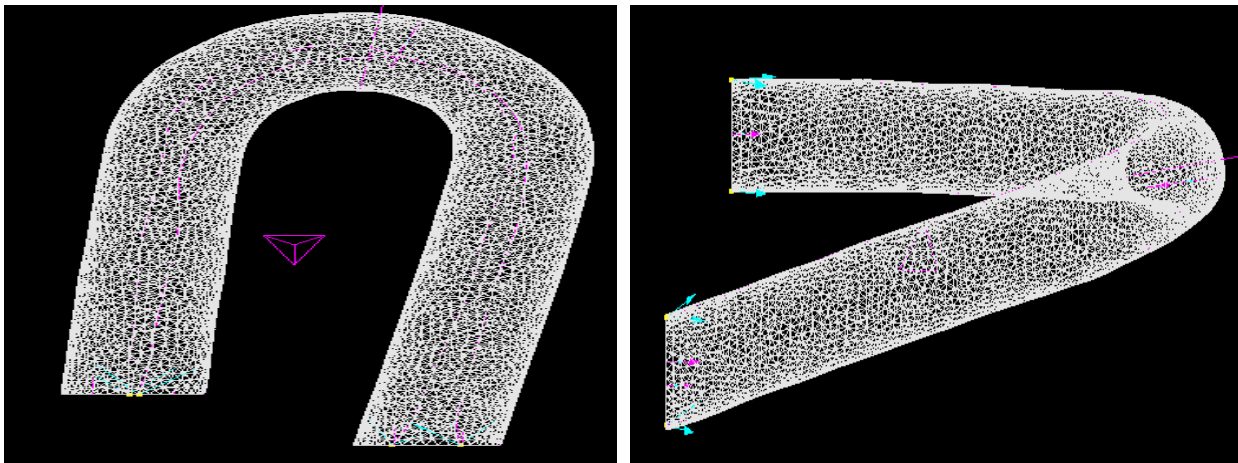

Figure 1: Aortic Flow Phantom (this does not appear to be an image of the flow phantom. Instead it looks like a surface mesh or stl file of the computational model. Additionally is this to a 1:1 scale, it appears distorted in my copy?)

The carotid bifurcation phantom used in this study is shown in Figure 2 and was designed based on the dimensions of a simplified carotid artery bifurcation. Unlike the aortic phantom this phantom is completely planar in orientation. The common carotid portion of the model had a specified ID of five eights of an inch (Same units comment here) with both the internal and external carotid arteries having a specified diameter of half of an inch. A three quarter inch long bulb with a three quarter inch ID was also specified for the left branch of the phantom. The branches of the internal and external carotid arteries were set at an angle of 60 degrees to one another. (It should be noted that like the aortic phantom the actual IDs were approximately three one hundredths of an inch undersized when compared to the specified dimensions.)
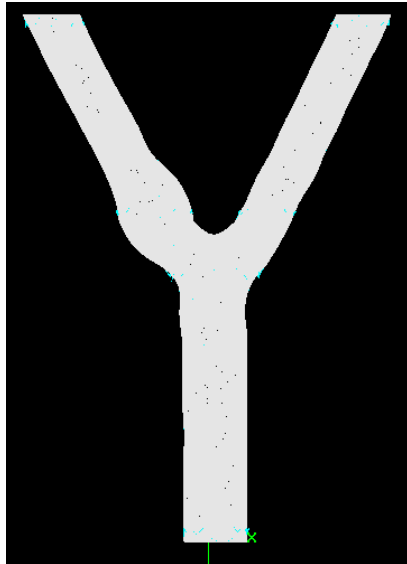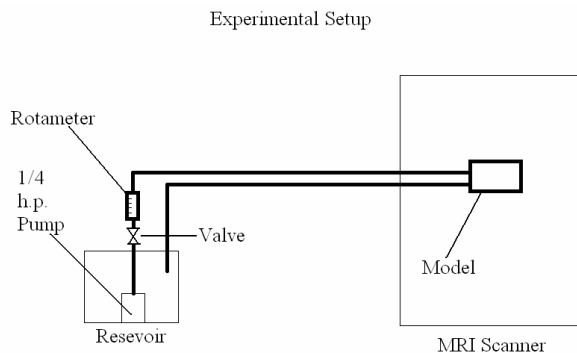

Figure2: Carotid Bifurcation Phantom   (same comment on this image of the bifurcated Phantom).   **Figure 3**: Experimental Flow Loop

Both phantoms were set in polycarbonate boxes in order to allow for the phantoms to be surrounded by water during the imaging process and were connected to the flow loop illustrated in figure 3.   A one quarter horse power pump (Flotec; Delavan WI) was used to provide steady flow throughout the flow loop. The flow rate was controlled through the use of a valve set distal to the pump in the flow loop and was set and monitored using a rotameter (Dakota Instruments; Orangeburg, NY) that was placed in-line after the valve in the loop. Flow rates of 1.7 L/min and 3L/min (Reynolds Number = 1600 and 3000 respectively) were used for the aortic flow phantom experiments and flow rates of 0.9 and 1.7L/min (Reynolds Number 1200 and 2500 respectively) were used in the carotid bifurcation experiments. Water was the working fluid used for both phantoms in both the CFD and MRI experiments.

2.2 MRI Imaging

Both the aortic and the carotid phantoms were imaged using a 1.5 Tesla Siemens Sonata MRI Scanner to obtain both geometric data for computational model reconstruction as well as velocity data for use as boundary conditions for the computational model and as validation for the computational model.   Gradient Echo acquisitions were used to obtain both the geometric and the velocity data.

2.2.1 Geometric Image Acquisition

The acquisition of images to construct the computational model of the aortic flow phantom was split into two parts. The first part involved acquiring the images for the ascending and descending portions of the model and the second part involved obtaining the images that would be used to reconstruct the arch. The information for the ascending and descending portions of the model was acquired through a series of transverse slices. It was found that a total of twenty 5mm thick transverse slices was needed to accurately reproduce the geometry of the ascending and descending portions

of the phantom. In order to reproduce the arch portion of the aortic phantom a series of transverse oblique and sagital oblique slices was obtained by placing a transverse slice at the top of the base of the arch in both the ascending and descending vessel and obtaining a 3mm thick slice every time this slice was rotated 5 degrees about a central point. A total of thirty five of these 3mm thick oblique slices were required to reconstruct the arch. The geometric images for the aortic flow phantom were obtained using two different base resolutions (256x256 and 512x512) for the same field of view 256x256mm. This translated into a resolution of 1mmx1mm pixels for the 256x256 base resolution and 0.5mmx0.5mm pixels for the 512x512. After processing the two different sets of images it was found that the higher resolution was not necessary for either of these models and this set was not used in the reconstruction of the aortic computational model (is it necessary to say this, or can this be said in the results discussion section?).

The geometric image acquisition for the bifurcation model was not as complicated because of the planarity of the model. It was found that a total of twenty four 5mm thick transverse slices and one 3mm thick coronal slices were sufficient to accurately reproduce the geometry of the bifurcation flow phantom (how was it determined that 24 slices were sufficient?). The base resolution for these slices was set at 256x256 with a field of view of 256mm x 256mm.

2.2.2 MRI Velocity Image Acquisition

Velocity data for both phantoms was obtained under steady flow conditions for a high and a low flow rate. In the case of the aortic phantom a total of nine velocity phase maps were acquired using gradient echo acquisitions. The location of the velocity phase maps can be seen in figure 4. In addition to the locations illustrated in figure 4 velocity phase maps were also obtained at the inlet for the inlet boundary condition, and at the centerline for both the ascending and descending portions of the phantom. The resolution of these images was 256x256mm and a slice thickness of 3mm was used. Three images were obtained for each of the three velocity dimensions. The TR and TE values were set so that the shortest TR and TE were used for each acquisition. The shortest TR and TE varied depending on the direction of the phase encoding. The Venc number was set at 30cm/s for all acquisitions.
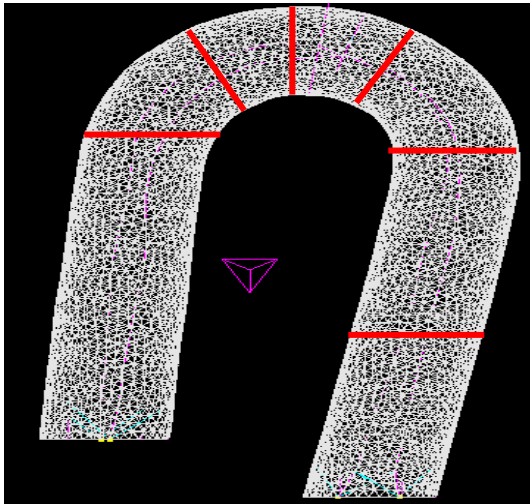

Figure 4: Velocity Measurement Locations
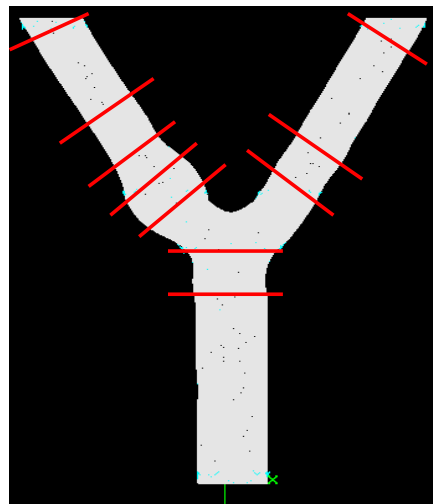Aortic Flow Phantom

Figure 5: Velocity Measurement Locations
Carotid Bifurcation Phantom

IF these planes are the same as used in the results section to illustrate the velocity profiles, I suggest that they annotated in some way to illustrate the postions. This will go a long way toward clarity of the velocity profile locations. Otherwise it is confusing.

A total of twelve velocity-phase maps acquired using the same imaging protocol outlined for the aortic flow phantom were acquired for the carotid bifurcation phantom. The location of the phase maps can be seen in figure 5. In addition a velocity phase map was acquired at the inlet and at the centerline of the flow phantom. As mentioned the imaging

protocol was the same as that outlined earlier the only difference was a Venc number of 60 cm/s was used in conjunction with the 1.7L/min flow rate.

2.3 Geometric Image Processing and Model Reconstruction

2.3.1 Geometric Image Processing

All of the images containing the geometric data from both phantoms were processed using the freeware program ImageJ (National Institute of Health (NIH)) in conjunction with the plug-in entitled Spline Snake (Matthews Jacob, University of Illinois at Urbana Champaign)[15]. The plug in spline snake uses a snake algorithm to segment the lumen boundary within the image. The Spline Snake program returns "X" and "Y" point data with the "Z" coordinate being encoded in the position of the slice relative to the other slices.

2.3.2 Model Reconstruction

The X, Y, and Z coordinates generated using the plug in Spline Snake were imported on an slice by slice basis into the 3D modeling software program Rhinoceros (Robert McNeel and Associates; Seattle WA). A closed curve was fit to the imported points, and a smoothing algorithm was applied to the resulting curve. In the case of the aortic flow phantom once all of the curves obtained from the transverse and oblique slices were complete a surface was lofted through the curves and a second smoothing algorithm was applied to smooth the surface. In the case of the carotid bifurcation flow phantom, a similar method was used with the addition of interpolated curves to connect the parent (common carotid) vessel to the daughter vessel. Once the surfaces of the vessels were completed, the surfaces were exported to the commercial Computational Fluid Dynamics preprocessor CFD GEOM (CFDRC; Huntsville AL). The accuracy of the resulting computational models will be further discussed in the Results section.

The idealized models of the flow phantoms were constructed solely in CFD GEOM using only the dimensions supplied to the manufacturer for the phantoms. As only the dimensions were used no smoothing algorithms or special treatment was needed for these models.

All models were meshed in CFD GEOM using an unstructured tetrahedral mesh. The unstructured tetrahedral mesh was applied in a two step process. In the first step, the meshing algorithm created an isotropic surface triangulation on trimmed NURBS surface. In the second step, the algorithm used a hybrid Delaunay/Advancing-Front technique to generate a tetrahedral grid within the model.[16] Several meshes of different finenesses were generated for each phantom in order to test the computational models for grid dependency and to allow for the comparison of the models generated from MRI data to the idealized models generated only from dimensions. For the aortic computational model generated from MRI data grids containing 121,154 cells, 303,285 cells and 1,419,491 cells were generated. In the case of the idealized model a single grid containing 322,233 cells was generated. For the MRI base carotid bifurcation computational model grids containing 121,819 cells, 318,855 cells, 469,890cells and 1,474,209 cells were generated. Only a single grid was generated for the idealized model containing 322,233 cells.

2.3.3 Velocity Phase Map Processing

The velocity phase maps acquired during the image acquisition step were processed using the software package Transform (Research Systems; Boulder CO). The phase information contained within the phase images was converted to velocity using equation (1)

Velocity (cm/s) = (Phase Value – 2047)*VENC/2047   (Eq. 1)

Each new image generated from velocity data had to be processed by hand in which all of the values outside of the flow field were set to zero in order to obtain the velocity flow field of interest. The velocity information obtained in this processing step was used to set the inlet boundary condition for both computational models as well as to provide the information necessary to validate the computational models in terms of the MRI measurements.

2.4 Computational Fluid Dynamics Simulations

The Continuity and Navier Stokes equations were solved using the commercial CFD program CFD ACE (CFDRC; Huntsville AL) using the finite element method. The inlet boundary condition for both models was obtained directly from an MRI phase map located at the inlet of the model it was assumed that the inlet velocity. The phase map was processed as described above and the velocity information for the inlet was converted into an array and imported as raw data into the CFD ACE solver. The data once imported was then fit to the inlet face and the individual boundary cells of the computational model using a linear interpolation algorithm. The inlet array for the aortic model contained 451 data points for both the 1.7L/min and 3.0L/min flow rates. The inlet array for the bifurcation model contained 145 data points for both the 1.7L/min and 0.9 L/min flow rates. The same flow rates used for the MRI based models were used on the idealized model. The operating conditions were the same for both models. Water was set as the working fluid (density = 997 kg/m^3, viscosity = 0.00855 kg/ms). The reference pressure was set to atmospheric (100000 N/m^2). The outlet boundary conditions were set at a constant pressure equal to the reference or atmospheric pressure.

3. RESULTS

3.1 Geometric Accuracy

The geometric accuracy of the computational models constructed from MRI images was determined by comparing the apparent diameters obtained from cross sectional areas of the reconstructed model in Rhinoceros to the apparent diameters (How is apparent diameter defined?) obtained from areas measured using ImageJ. The resulting diameters were then compared with actual measurements taken where possible in the straight sections of the models. The apparent diameters of the reconstructed models agreed with the apparent diameters measured from MRI images to within 0.5mm (what is the percentage difference relative to the actual diameter of the flow phantom, not the design diameter?)for all measurements in both models. Agreement between the physical measurements of the glass models and the computational models also agreed to within 1/32 of an inch (mixed units). Does the previous discussion address the accuracy of the entire construction or should we be concerned with the cross-sectional aspect ratio, the centroid of each cross-section and the resultant model centerline as a means of looking at the accuracy of the axial construction?

3.2 Accuracy of Velocity Predictions

The accuracy of the computational models for both phantoms was evaluated qualitatively by comparing the flow patterns observed in the MRI measurements to the flow patterns generated in by the CFD models. Specifically the vector plots of the in-plane velocity components corresponding to the locations of velocity data acquisitions as seen in figures 4 and 5 were compared to the corresponding MRI generated vector plots, the results are presented in the following figures. (Figures 6, 7&8 refer to the aortic phantom. Figures 10, 11, &11 refer to the bifurcation phantom)
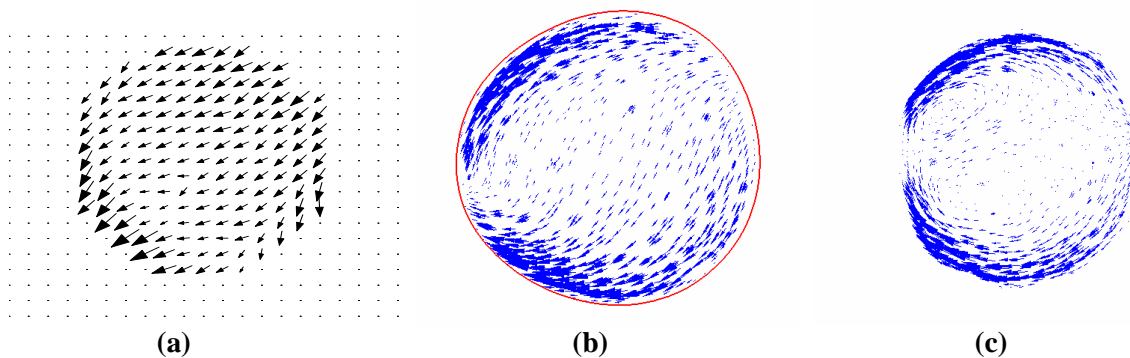

(a)	**(b)**	**(c)**

Figure 6: In-plane Velocity Vector Plots taken at 45 degrees to the left of the center of the arch (Flow Rate = 3.0L/min) (a) =MRI generated Vector Plot (b) =CFD generated Vector Plot (c) =Idealized Geometry generated Vector Plot For any vector plot, a reference vector should be provided so that the reader can see the relative velocity magnitudes, not providing one can give flase impressions regarding the strength of these secondary flow patterns.
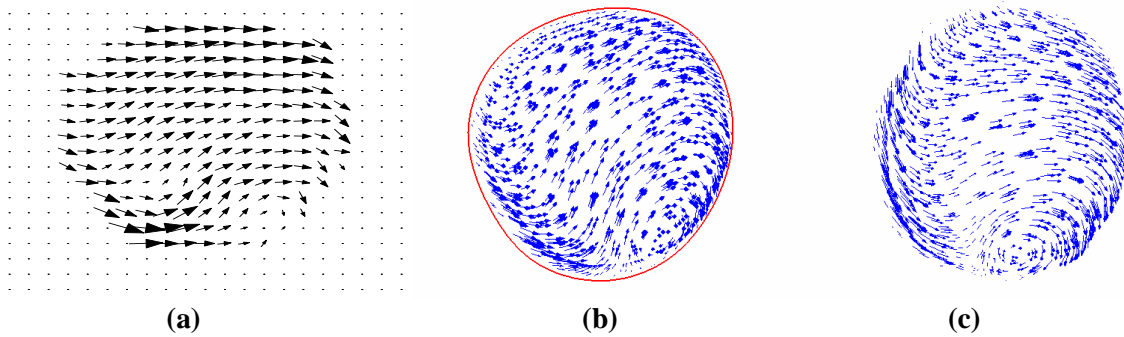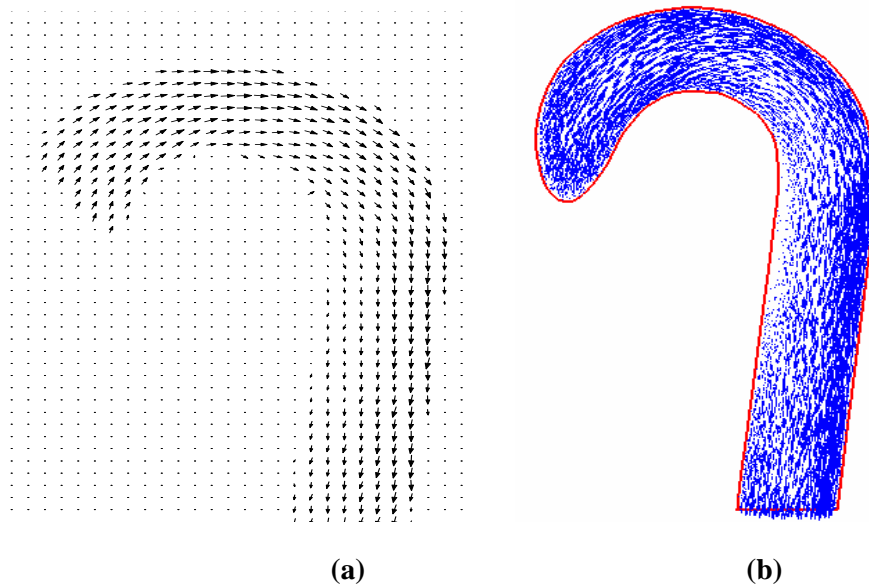
Figure 7: In-plane Velocity Vector Plots taken at the center of the arch (Flow Rate = 3.0L/min) (a) =MRI generated Vector Plot (b) =CFD generated Vector Plot (c) =Idealized Geometry generated Vector Plot
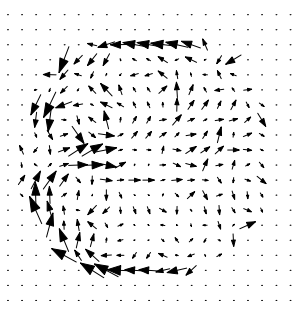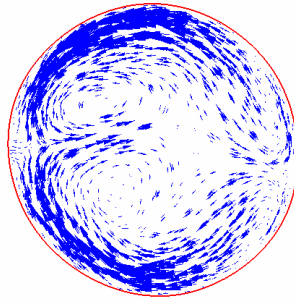

Figure 8: In-plane Velocity Vector Plots taken at the centerline of the descending vessel of the aortic flow phantom (Flow Rate = 3.0L/min) (a) =MRI generated Vector Plot (b) =CFD generated Vector Plot The scales of these two figures do not look the same, can we correct?

The above figures show good qualitative agreement when the flow patterns predicted by both the MRI generated computational model and the idealized geometry computational model are compared to MRI measurements for the aortic flow phantom. The flow patterns seen in a slice taken at 45 degrees to the left of the center of the model (these cutting planes should really be specified on one to the overall models so that the reader can visually see where you are describing. (figure 9) show that both computational models predict that the in-plane velocity vectors will be strongest along the outside wall with the top half of the vectors moving in a counter clockwise direction and the bottom half of the vectors moving in a clockwise direction indicative of swirling flow which is confirmed by the vector plot generated from MRI data. (This secondary flow formation is know as a dean cell and is made up of two counter rotating vorticies. It results from the fact that the curved path of the flow. You might want to look into calculating the Dean number as a reference value. Note that one of the vortices may be stronger than the other due to non-circular cross section or compound vessel curvature.   In the slice taken at the center of the top (figure 10) of the arch similar agreement is seen with all models showing a predominant left to right flow with a small vortex seen in the bottom right hand portion of the slice. Similar agreement between the two computational models and the MRI measured velocity patterns is also seen in a slice taken along the centerline of the descending portion of the aortic flow phantom (figure 9 the idealized geometry is not shown due to spatial constraints) in both the computational model and the MRI generated vector plots a zone of low flow is seen just after the arch as the descending portion of the aortic flow phantom curves towards the left.
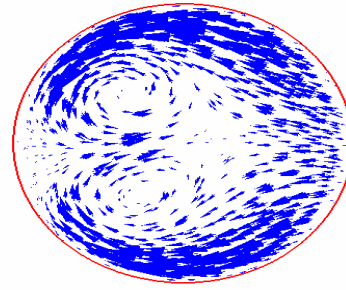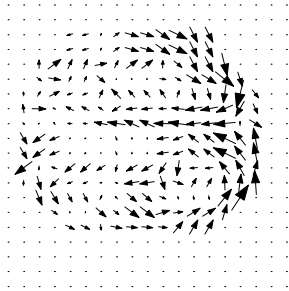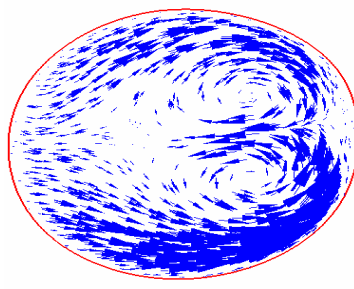
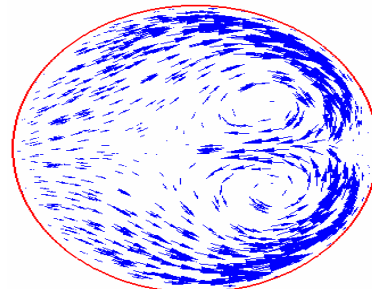**(a)** **(b)** **(c) why is this one oblong, is it not normal to the flow**

Figure 9: In-plane Velocity Vector Plots taken in the bulb of the left branch of the carotid bifurcation phantom (Flow Rate = 1.7L/min) (a) =MRI generated Vector Plot (b) =CFD generated Vector Plot (c) =Idealized Geometry generated Vector Plot The differences in scales make the comparison difficult here.

(a) **(b)** **(c)**

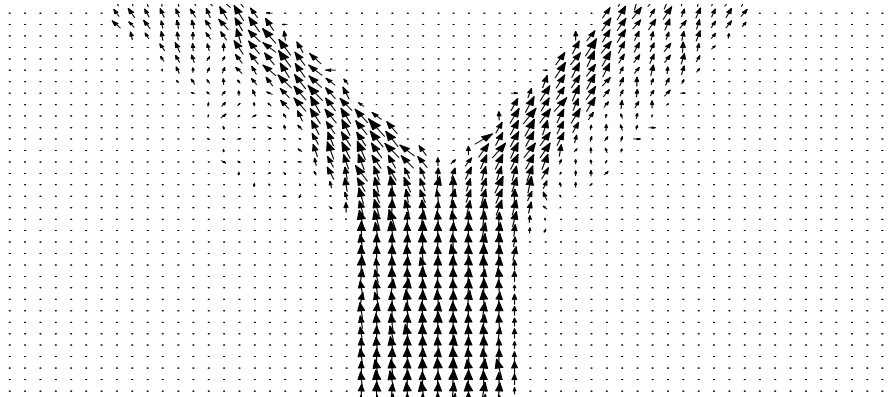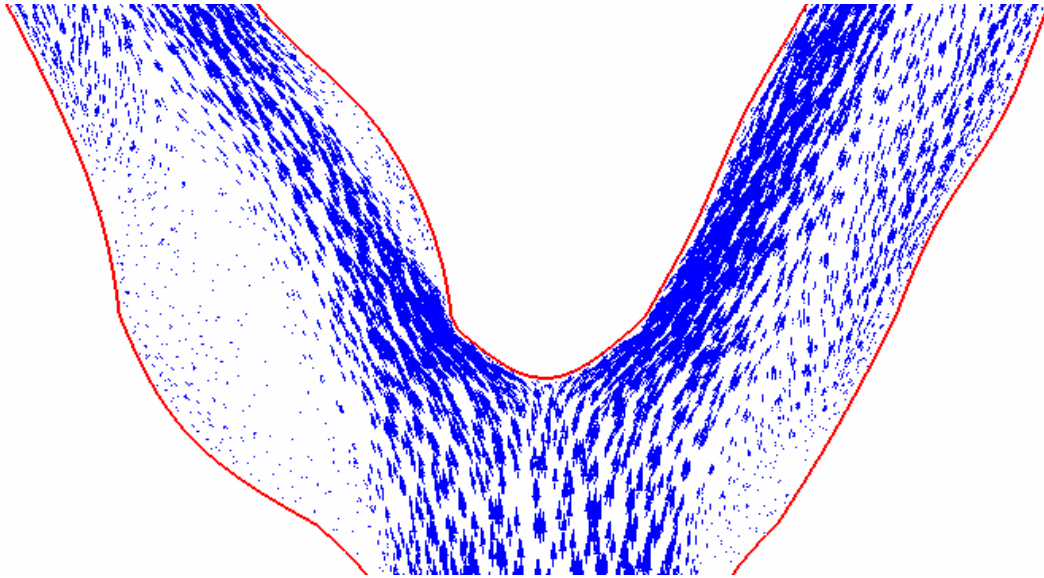**Figure 10:** In-plane Velocity Vector Plots taken in the right branch of the carotid bifurcation phantom approximately 70mm from the inlet (Flow Rate = 1.7L/min) (a)=MRI generated Vector Plot (b)=CFD generated Vector Plot (c)=Idealized Geometry generated Vector Plot

(a)

(b)

Figure 11: In-plane Velocity Vector Plots taken from a planar slice located at the center of the phantom (Flow Rate = 1.7L/min) (a) =MRI generated Vector Plot (b) =CFD generated Vector Plot A good comparison cannot be made with the varying scales of these tow figures.

Good qualitative agreement was also seen in the case of the carotid bifurcation phantom. In a slice taken within the bulb of the bifurcation model (figure 10) both the idealized and MRI generated computational models predict that vortices will form towards the left side of the bulb with strong flow patterns seen along the outer wall of the model with flow along the top half moving in a counter clockwise direction and flow along the bottom half moving in a clock wise direction. Similar flow patterns are seen as well in the right branch of the carotid bifurcation except the directions are reversed. Now the vortices are located to the right side of the vessel with the outer flow patterns moving in a clockwise direction for the top half of the vessel and in a counterclockwise direction in the bottom half of the model. Good qualitative agreement was also seen in a slice taken along the centerline of the bifurcation phantom a portion of which is seen in figure 11 (Idealized geometry not shown). The computational model predicts that areas of high velocity will be localized along the inner walls of the bifurcation model after the parent vessel splits into the two daughter vessels with lower velocity values concentrated along the outer walls of the bifurcation after the split. These observations are consistent with the velocity patterns generated from the actual MRI data.

Quantitative agreement was evaluated by taking a magnitude velocity profile every 10mm along the centerline of both the aortic and bifurcation models. (Selected results for the aortic model are shown in figure 12, and selected results for the bifurcation model are shown in figure 13. Note the idealized geometry results are not shown for the sake of clarity.) In order to match the CFD data set the CFD velocity value was interpolated from surrounding data points. The MRI velocity data was calculated by taking the average of the point of interest and the surrounding eight points. (This a comparison of spatial averaging at discrete locations over a defined area (MRI) to an interpolated point value (CFD) is questionable and could skew your results. This should be considered.) In the case of the aortic model it was necessary to include velocity profiles taken from the slices used to generate the flow pattern data due to the non-planarity of the model. This data was used to quantitatively evaluate the flow in the arch of the model. Qualitatively, the flow profiles predicted by the computational models were very similar in shape to the flow profiles generated from MRI data. Both the ideal and the MRI generated computational models correctly predicted that in the aortic phantom the flow profiles in the ascending vessel would show higher velocities along the left hand wall of the model and would flatten out as the profiles approached the arch. Both models also correctly predicted that in the arch at 45 degrees to the left of center the flow profiles would flatten out before showing that higher velocities would be concentrated along the outer wall as flow proceeded through the arch and into the descending portion of the aortic phantom.   In the bifurcation phantom the computational models were also successful in predicted the shape of the centerline velocity profiles. Both

the idealized and the MRI generated model correctly predicted that the flow would become almost parabolic in the parent vessel before taking on an "M" shaped velocity profile in the portion right before the parent vessel splits into the two daughter vessels. Both models (phantom and CFD?) also correctly predicted that after the split the velocity profiles would be skewed with higher velocities occurring near the inside wall of each of the branch vessel with the amount of skew decreasing as the flow approached the outlet of the model since they are both correctly predicting this feature, we should reference something that points that feature out..

While it is unwieldy to conduct a point by point evaluation to see how each predicted velocity data point compares to the measured value for the entire model it is more reasonable to do so for the predicted values used for the centerline velocity profiles. In the case of the aortic flow phantom, the predicted velocity values differed from the measured values by on average 0.72 cm/s for the MRI generated computational model and 0.66 for the Idealized geometry computational model. The closest agreement both qualitative and quantitative was seen in the ascending portion of the model where the velocity values differed on average by 0.43 cm/s for the MRI generated geometry and 0.32 for the idealized geometry. The models showed the least amount of agreement in regions of complex flow. In the case of the MRI generated model the location of least agreement occurred at the center of the arch where the velocity data points differed on average by 1.6 cm/s. However, the velocity profile closely resembles the profile generated from the MRI data except that the velocity values are larger in the predicted model then the values measured via MRI. In the case of the idealized geometry the poorest agreement occurred at a location 45 degrees to the right of the center of the arch where the velocity data points differed on average by 1.4 cm/s.

Similar results were also obtained in the case of the bifurcation flow phantom. The predicted velocities in this case differed from the MRI measured velocities by 0.99 cm/s in the case of the MRI generated computational model and 0.95 cm/s in the case of the idealized computational model. Once again the closest agreement was obtained in areas of simple flow patterns namely in the parent vessel where the predicted values differed by 0.30 cm/s on average for the MRI generated model and 0.7 cm/s in the case of the idealized geometry. The areas of least agreement again corresponded to areas of complex flow patterns. In both the MRI generated model and CFD generated model the areas of least agreement occurred at 70 mm from the inlet in the right branch where on average the predicted velocities differed from the measured velocities by 2.0 cm/s on average in both the idealized and MRI generated models.

Figure 12: Centerline Velocity Profiles Aortic Flow Phantom Without a scale or other means of specifying locations of these positions, it is difficult to visualize the flow.
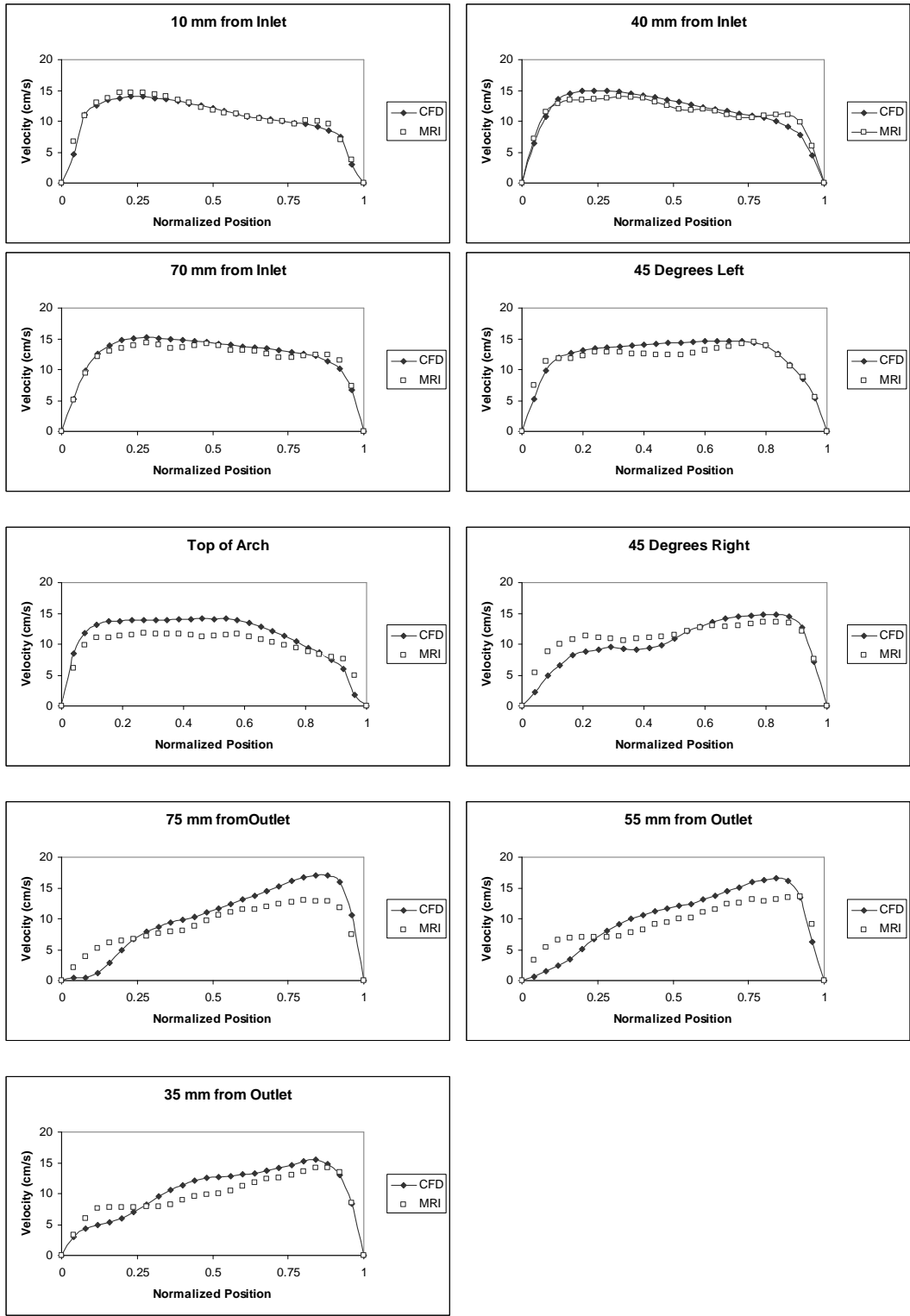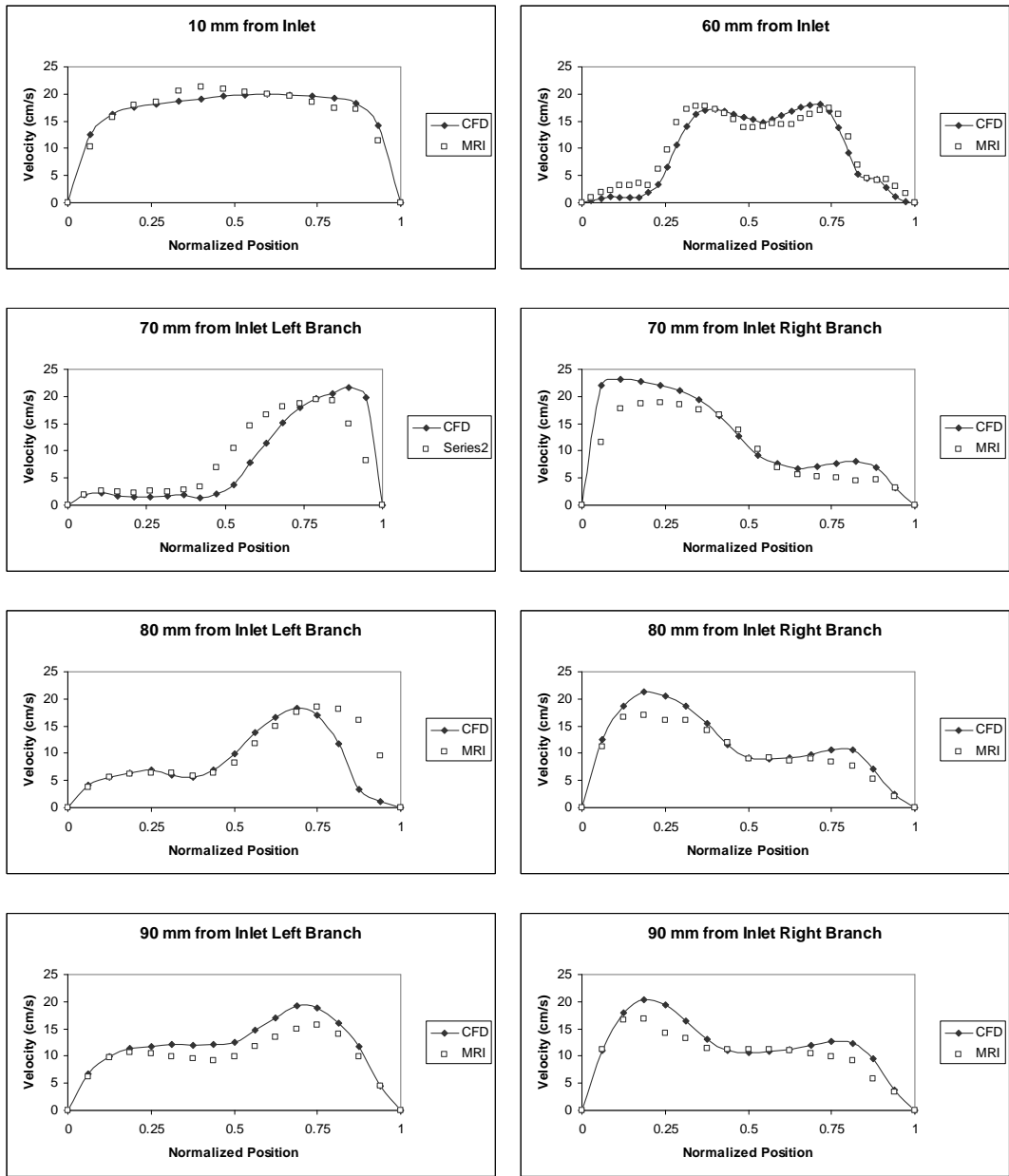
Figure 13: Centerline Velocity Profiles for Carotid Bifurcation Flow Phantom

4: DISCUSSION

The presented results indicate that computational models can accurately predict or reproduce the flow patterns and velocity distributions seen an ideal model both qualitatively and quantitatively. In the above experiments the computational models were constructed using two methods. In the first method the models were reconstructed from X, Y and Z data gathered from MRI images taken for that purpose. The second method relied solely on dimensions given to the manufacturer prior to the construction of the models. In both phantoms the flow fields were accurately predicted by models constructed using the MRI based method The models used in this experiment are oversimplified reproductions of the in-vivo situation and as such were easy to reconstruct using a few dimensions. In the case where actual blood vessels are to be model it has been shown by several previous studies that MRI generated models can accurately reproduce the flow fields seen in the blood vessel qualitatively and this would be the preferred method to use in further work and in in-vivo situations. The biggest difficulty that arises in using this method is the time required and the number of images required to accurately reconstruct a specific geometry. In this study, fifty-five images were required to reconstruct the aortic phantom. The acquisition time for obtaining these images under ideal conditions took longer than one hour to complete an in-vivo thoracic aorta including the sub-clavian and common carotid arteries would require a good deal more images in order to incorporate the highest degree of detail into the model as possible in order to obtain the most accurate predictions or simulations (may require multi-modal imaging?). This would have to be accomplished while accounting for the synchronization of image acquisition with the heart beat thus adding more time as well as having to deal with patient motion resulting from having to lie in a scanner for an extended period of time.

The velocity magnitude was used in the effort to quantify the agreement between the computational models and MRI measurements as this method would eliminate the need to account for the angle of the flow seen in the MRI measurements in the comparison. One of the difficulties arising when trying to compare the individual components of velocity measured in MRI to those predicted by CFD is that the components are not generated using the same coordinate system. When velocity is measured in the MRI and the slice in which the measurement is taken is angled the velocity coordinates are encoded in directions that are also shifted to correspond with the angle of the slice. As a result the velocity components obtained from the MRI measurements must be corrected for the angle at which they are encoded in order to align the velocity components with the global coordinate system used by the CFD program. By using the magnitude velocity in which all three components are accounted for but the direction of the vectors is ignored eliminates the need to account for the angle at which the MRI velocity vectors were encoded. It should be noted that this was done for both models considering only the main velocity component with similar results, good qualitative agreement was seen for both models however quantitatively this method was slightly less accurate in that the average difference between the measured velocity data points and the predicted values was slightly higher when velocity components are compared for both models

In both models, it was noted that as flow approached the outlets the predicted velocities from the models tended to be higher than the velocities actually measured (this may be an effect of the post processing as well, see previous discussion). In the simulations, the outlet pressure was set to atmospheric pressure; however there was no way to determine the actual pressure at the outlet. It is possible that the pressure at the outlet may have been slightly greater than atmospheric pressure and thus causing the lower flow values.

5: CONCLUSIONS

Computational Fluid Dynamics can be used to accurately model flow patterns in a real world situation both qualitatively and quantitatively. The above work represents the first step in a series of steps that will continually introduce variables into the models and validate the results of these models as the variables are included for accuracy. More complex models are required in order to determine if the above detailed method can be used to accurately model blood flow in an in-vivo situation. However the above methods for both imaging and modeling must will need to be modified in order account for more complex flow situations. In conjunction with this work additional work must be done in order to determine which variables and quantities need to be monitored and measured in order to tailor a method that can be used as a prognostic tool for use on potential astronauts.

REFERENCES

1) *The Vision for Space Exploration* February 2004 National Aeronautics and Space Administration NP-2004-01-334-HQ

2) R.J. White, J.B. Bassingthwaighte, J.B. Charles, M.J. Kushmerick and D.J. Newman; Issues of Exploration: Human Health and Wellbeing During a Mission to Mars *Advances in Space Research* **31**, 7-16, 2003

3) D.A. Steinman; Image Based Computational Fluid Dynamics Modeling in Realistic Arterial Geometries *Annals of Biomedical Engineering* **30**, 493-497 2002

4) D.A. Steinman, J.B. Thomas, H.M. Ladak, J.S. Milner, B.K. Rutt and J.D. Spence; Reconstruction of Carotid Bifurcation Hemodynamics and Wall Thickness Using Computational Fluid Dynamics and MRI *Magnetic Resonance in Medicine* **47**, 149-159 2002

5) Q. Long, X. Yun Xu, B. Ariff, S.A. Thom, A.D. Hughes, and A.V. Stanton; Reconstruction of Blood Flow Patterns in a Human Carotid Bifurcation: A Combined CFD and MRI Study *Journal of Magnetic Resonance Imaging* **11**, 299-311 2000

6) R. Botnar, G. Rappitsch, M.B. Scheidegger, D. Liepsch, K. Perktold, and P.Boesiger; Hemodynamics in the Carotid Artery Bifurcation: A Comparison Between Numerical Simulations and In-Vitro MRI Measurements *Journal of Biomechanics* **33**, 137-144 2000

7) S.Z. Zhao, X.Y. Xu, A.D. Hughes, S.A. Thom, A.V. Stanton, B. Ariff, and Q. Long Blood Flow and Vessel Mechanics in a Physiologically Realistic Model of a Human Carotid Arterial Bifurcation *Journal of Biomechanics* **33**, 975-984 2000

8) I. Marshall, S. Zhao, P. Papathanasopoulou, P. Hoskins, and X. Yun Xu MRI and CFD Studies of Pulsatile Flow in Healthy and Stenosed Carotid Bifurcation Models *Journal of Biomechanics* **37**, 679-687 2004

9) A. Leuprecht, S. Kozerke, P. Boesiger, and K Perktold Blood Flow in the Human Ascending Aorta: A combined MRI and CFD Study *Journal of Engineering Mathematics* **47**, 387-404 2003

10) N.B. Wood, S.J. Weston, A.D. Gosman and D.N. Firmin Combined MR Imaging and CFD Simulation of Flow in the Human Descending Aorta *Journal of Magnetic Resonance Imaging* **13**, 699-713 2001

11) F.P. Glor, J.J.M. Westenberg, J. Vierendeels, M. Danilouchkine, P. Verdonck Validation of the Coupling of Magnetic Resonance Imaging Velocity measurements with Computational Fluid Dynamics in a U Bend Artificial Organs 26, 622-635 2002

12) Q. Long, X.Y. Xu, M. Bourne, and T. M. Griffith Numerical Study of Blood Flow in an Anatomically Realistic Aorto-Iliac Bifurcation Generated from MRI Data *Magnetic Resonance in Medicine* **43**, 565-576 2000

13) J.A. Moore, B.K. Rutt, S.J. Karlik, K. Yin, C. R. Ethier Computational Blood Flow Modeling Based on In Vivo Measurements *Annals of Biomedical Engineering* **27**, 627-640 1999

14) S.Z. Zhao, P. Papathanasopoulou, Q. Long, I. Marshall, and X.Y. Xu Comparative Study of magnetic Resonance Imaging and Image-Based Computational Fluid Dynamics for Quantification of Pulsatile Flow in a Carotid Bifurcation Phantom *Annals of Biomedical Engineering* **31**, 926-971 2003

15) M. Jacob, T. Blu, and M. Unser Efficient Energies and Algorithms for Parametric Snakes *IEEE Transactions on Image Processing* **13**, 1231-1244

16) CFD GEOM Manual CFD Research Corporation Huntsville AL